Desalination and Water Treatment
www.deswater.com
doi: 10.5004/dwt.2020.25147

182 (2020) 13–27
April

CFD study on the performance of hollow fiber ultrafiltration membrane modules with different fiber arrangement

Liwei Zhuang*, Gance Dai, Zhen-liang Xu

State Key Laboratory of Chemical Engineering, East China University of Science and Technology, Shanghai 200237, China, Tel. +86 2164253670; email: lwzhuang@ecust.edu.cn (L. Zhuang), Tel. +86 2164252353; email: gcdai@ecust.edu.cn (G. Dai), Tel. +86 2164252989; email: chemxuzl@ecust.edu.cn (Z.-l. Xu)

Received 27 May 2019; Accepted 10 November 2019

ABSTRACT

Effect of fiber arrangement on the performance of hollow fiber ultrafiltration membrane modules has been studied using computational fluid dynamics (CFD) method. Four fiber arrangement modes, namely sparse to dense radially, dense to sparse radially, random and uniform, have been considered in the present study by developing dedicated CFD models. The fluid flow and fouling behavior inside the hollow fiber membrane modules have been simulated. The time-dependent velocity and pressure distributions have been presented for each module. The proportion of energy consumed by the inlet manifold decreased while the one by fiber bundle increased. The module with fiber arrangement sparse to dense radially had higher energy efficiency than the other three modules. In each module, the region where fibers had extreme fiber average flux tended to migrate with time. At the end of filtration, the fibers with highest fiber average flux were the ones with originally lowest fiber average flux and vice versa. However, the overall distribution of fiber average cake mass, which had the similar profile of original flux distribution, underwent little change. The mathematical model, consisting of geometrical and operating parameters, can be applicable to describe the water productivity of hollow fiber membrane modules with different fiber arrangement.

Keywords: Hollow fiber membrane module; CFD; Fiber arrangement; Energy efficiency; Fouling

1. Introduction

Hollow fiber membrane modules (HFMMs) have been used in a wide range of separation applications [1–4]. To realize the industrialization of HFMMs, sufficient understanding is required prior to improving the performance of HFMMs during operation. Therefore, the fluid mechanics and mass transfer within the HFMM should be systematically studied. However, it is difficult to conduct research based on the entire HFMM. Thousands of fibers are densely packed inside the module to form shell and lumen micro-channels with momentum and mass transfers. The invisible space with complex transport process causes challenges to experimental methods. Generally, the performance of entire HFMM is estimated with the assumption that fibers have the same size and are uniformly spaced [5–7]. In addition, the fluid flow is assumed to be uniform in any cross-section of shell and lumen sides. The performance of HFMM with ideal structure can be determined through the analysis of single fiber.

However, HFMMs are not "ideal" devices. One of most pronounced non-idealities is the non-uniform packing of fibers. The random packing causes a wide range of shell channel sizes and therefore the shell fluid mal-distribution. Thousands of fibers are exposed to different hydrodynamics condition and will possess various separation properties. Hence, the entire HFMM may have non-ideal performance, which deviates from the one based on single fiber prediction.

* Corresponding author.

In the past few decades, membrane researchers have carried out numerous studies to dig out how non-uniform packing affects the performance of HFMMs, attempting to eliminate the gap between lab research and industrial application. The early study by Noda et al. [8] was focused on counter-current hollow fiber dialyzers. The results showed that if fibers were sparsely packed to cause channeling flow, highly non-ideal behavior of dialyzer was observed. When the fibers in the module were packed in order, the dialyzer behaved nearly ideally. To visualize the fluid flow and concentration fields in the fiber bundle, non-invasive methods such as particle image velocimetry, computed tomography (CT) scanning [9,10] can be applied, or using residence distribution time [11] curve as an indirect method. To quantitatively analyze the non-uniformity of fiber packing, a series of mathematical and statistical models have been chosen to virtualize the fiber arrangement. Chen and Hlavacek [12] adopted Voronoi tessellation to model randomly packed hollow fiber bundles. Voronoi tessellation is widely applied [11,13–17] by using polygonal cells to represent the objects in random arrangement. The inter-boundary is equidistant between any two neighbor polygonal cells. Another popular method is the free surface model [18–20], which was first developed by Happel [21], treating the fiber bundle as a cell cluster. Each cell consists of a fiber and a surrounding annular fluid envelope. Both of the two methods above can be used to evaluate the module mass transfer coefficients with the individual cell mass transfer coefficient. The results of studies above showed that random packing of fiber was detrimental to the performance of HFMMs due to creation of channeling flow. As the literature [18,20] reported, the negative effect of random packing would get weakened as the packing density is increased, whereas other researchers [11] concluded that the non-ideal fluid flow became increasingly more serious as the packing density increased until it reached 50%, afterward the non-uniformity of fluid distribution would decrease slightly as the packing density increased. Some study [19] indicated that an increase in packing density would make mal-distribution more serious. The contradictions among the above studies probably result from the uncertainty in random packing, which covers all the possible modes of fiber arrangement. Therefore, the effect of fiber arrangement deserves further investigation. One can avoid using the Voronoi tessellation and free surface model by conducting computational fluid dynamics (CFD) simulation with simplification treatment, such as representing the entire fiber bundle with certain group of fibers [22], or applying porous media model with random porosity and hydraulic resistance [23], or developing novel CFD models [24] to account for the effect of channeling flow.

The effect of non-uniform fiber packing on the performance of HFMMs seems to be studied extensively. However, the related studies are all focused on membrane processes with driving force of concentration gradient, such as gas separation [25], dialysis [8], extraction [13]. During the modeling and simulation [13,15,16,23,24,26–30], the concentration-driven processes were assumed to be steady implicitly or explicitly, which is the case for real processes. As for the pressure-driven membrane processes, especially the dead-end filtrations, foulants continuously accumulate on the membrane surface, resulting in time-dependent fluid flow as the filtration resistance increases [7,31]. Hence, different non-ideal behavior is expected to occur during pressure-driven processes in HFMMs with non-uniform fiber packing.

To the best of our knowledge, the effect of non-uniform packing on the performance of HFMMs under dead-end filtration has not been studied previously, which will be the focus of the present study. In addition, different from most of the studies on HFMMs with random fiber packing [16,18–20,24,29,30,32], we will consider different fiber arrangement and try to find if there is one optimized mode that can improve the performance of HFMMs. CFD models will be developed based on our previous study [33] to investigate the time-dependent ultrafiltration in four industrial-scale HFMMs with different fiber arrangement. Comparisons of fluid distribution and fouling process among the four HFMMs will be made to analyze how fiber arrangement affects the filtration process of HFMMs.

2. Modeling development

2.1. Model description

In Fig. 1a, the HFMM is operated at dead-end outside-in mode. The operation conditions are presented near the inlet and outlet regions. During the filtration, the feed passes the inlet manifold, afterward it enters the shell space. 100% of the feed permeates the porous membrane, leaving the foulants accumulated on the membrane surface. The permeate is collected at the end of fiber bundle and exits from the outlet. The schematic of fiber bundle in the lower right corner of Fig. 1a represents the fiber arrangement in the HFMM. The non-uniformity of fiber packing at the inlet region results mainly from the local compression of fibers in the tubesheet to form channels to let feed pass. The rest of fiber bundle also suffers from mal-distribution, which is merely due to the poor handle of fiber packing process.

To facilitate the model development, several simplifications have been adopted regarding different part of the real HFMM. As shown in Fig. 1b, the inlet region is replaced with an inlet manifold. Both of them have the same function of causing initial mal-distribution and pressure drop. This simplification has turned the inlet region into structural domain which can be meshed with structural grids. Hollow fibers in the rest part of HFMM are assumed to be straight, rigid, uniformly sized and packed with certain distribution in the module.

The inlet manifold in Fig. 1b is developed in the basis of our previous study [34], which is focused on the structure optimization of inlet manifolds to offer uniform flow distribution and low energy consumption. The inlet manifold consists of 36 uniformly distributed regular hexagon (length of side: 4.5 mm) openings with a fractional hole area of approximately 21.4%. The internal diameter and length of the pressurized housing are 0.1 and 0.5 m, respectively. The internal/external diameter of the fibers is 0.7/1.3 mm, with the length of 0.5 m.

Figs. 2a–d present four modes of fiber arrangement, namely ideal (uniform packing), dense to sparse radially, sparse to dense radially and random. The first fiber arrangement has been applied in our previous study [33] to

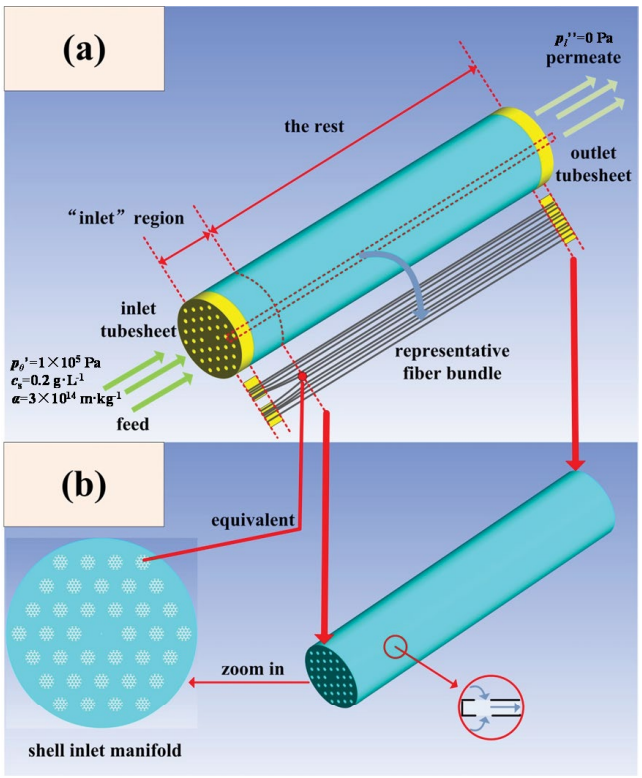

Fig. 1. Structure of the HFMM: (a) real module and (b) module for CFD simulation (adapted from literature [33]).

investigate the time-dependent fluid distribution and fouling process in an HFMM. Therefore, the simulation results of this case, as the benchmark of the other three cases, can be obtained directly without any simulation. Although the assumption of uniform fiber arrangement has been made in many numerical studies regarding single-fiber [35,36] or entire-module system [34,37], most of the HFMMs suffer from non-uniform fiber packing in practice. The second fiber arrangement shows that fibers are packed densely in the center of module and get increasingly sparser along the radial direction. This fiber arrangement is similar to the one in the early patent [38] assigned to Dow Chemical (Midland, Michigan, United States). The third fiber arrangement is a reverse mode of case 2, that is, fibers are packed sparsely in the center of module and get increasingly denser along the radial direction. The fourth fiber arrangement, that is, the random packing, is the most common one in practical application. Strictly speaking, the hollow fibers in the fourth HFMM were not completely randomly packed due to the presence of periodic fiber bundles. In literature, the performance of HFMM with random fiber packing can be predicted by statistically analyzing the property of every single fiber thereof, which means the overall performance of module is a function of the property of all the individual fiber [17,18]. There could probably be fibers with close/identical properties regardless of their relative positions. In the basis of the aforementioned possibility, the entire module could be simplified into certain parts of units with close/identical performance, which enables us to perform the same simplification of model development as we did to the other three cases.

The numbers of fibers in the four HFMMs presented in Fig. 2 are 2,682; 2,556; 2,742 and 2,508, respectively. The packing density of the four HFMMs is in the range of 42.4%–46.3%.

The hollow fibers in the cylinder for the four HFMMs were artificially arranged in certain mode, thus enabling the entire computational domain to be divided into 12 identical sub-domains. With the treatment above, for purpose of reducing computational burden, only one-twelfth of the HFMM was selected for simulation, as shown in Fig. 3. The computational domain in Fig. 3a has approximately 2.27 × 10^6, 2.21 × 10^6, 2.24 × 10^6, 2.19 × 10^6 structural grids for the four HFMMs, respectively. Snapshots of the grids distribution in the three regions has been presented in Fig. 3b. The mesh strategy was determined by grid convergence index [39] check which was conducted in our previous study [34]. It is highly suggested that dedicated mesh refinement be performed in the region of shell/membrane and lumen/membrane interfaces, as has been done in literature [6,35]. The mesh resolution should also be dependent on the fiber packing density [40]. However, we have performed simulation of fouling behavior in small-scale HFMMs with different meshing strategies. Little difference in the simulation results between different cases was observed. This is probably because the fouling in the simulation is highly dependent on the trans-membrane pressure (TMP) and the pressure in the present membrane system could be predicted with similar precision with fine or coarse meshes. Therefore, we can use the present meshing strategy to pursue the most industrially relevant results regarding HFMMs.

2.2. Conservation equations

For the four cases, the computational domain has three coupled sub-zones: lumen, shell zones and porous membrane zone. Three sets of conservation equations are solved

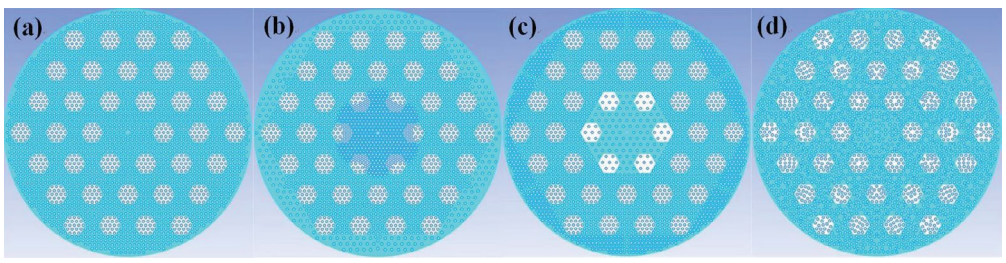

Fig. 2. Four modes of fiber arrangement inside the HFMMs: (a) ideal, (b) dense to sparse radially, (c) sparse to dense radially, and (d) random.

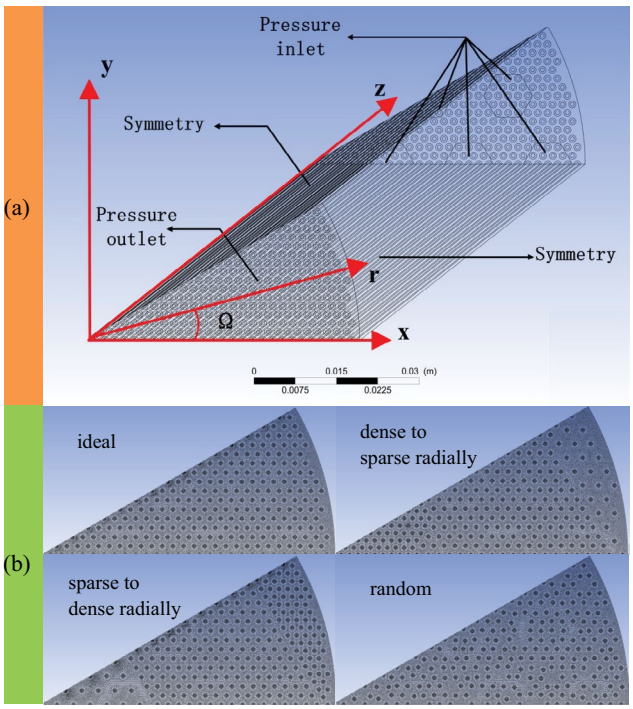

Fig. 3. One-twelfth of the HFMM as the computational domain (adapted from literature [33]). (a) The HFMM with uniform fiber packing was selected as the representative case to depict the computational domain. The annotations above represent the boundary conditions for solving the conservation equations. The mathematical expressions of the boundary condition can be seen in literature [33]. (b) The details of grid distribution from a cross section view.

with additional numerical treatment imposed on the zone–zone interface, thus enabling the entire details of momentum and mass transfer to be displayed. A transient, incompressible, Newtonian flow is considered in all the sub-zones. In the lumen side, the axial velocity is less than 0.1 m/s, as estimated with the initial volumetric flow rate. Therefore, the lumen Reynolds number is less than 70 with the fiber size of 0.7 mm, which makes the lumen flow laminar. Eqs. (1) and (2) are the continuity and Navier–Stokes (NS) equations, respectively.

$$\nabla \cdot \vec{v} = 0 \tag{1}$$

$$\rho \frac{\partial \vec{v}}{\partial t} + \nabla \cdot \left(\rho \vec{v} \vec{v}\right) = -\nabla p + \mu \nabla^2 \vec{v} \tag{2}$$

$\vec{v}$, ρ, p and μ are the fluid velocity, density, static pressure and dynamic viscosity, respectively.

In the shell side, based on the average inlet velocity through the manifold (estimated with the initial volumetric flow rate of HFMMs) and the size of the manifold channel, the manifold Reynolds number is approximately 1.1 × 10^3, whereas the shell Reynolds number is in the range of approximately 10~2 × 10^2, based on the area-average axial velocity near the manifold and the hydraulic diameter of the shell side. The standard k-ω turbulence model is applied in consideration of the presence of non-ideal flow field caused by local high fluid velocity, fiber-bounded and over-fiber transverse flow. The feasibility of present turbulence model applied to the shell flow has been discussed in detail and validated with experiments in our previous study [34]. The shell continuity and NS equations are given as follows:

$$\nabla \cdot \vec{v} = 0 \tag{3}$$

$$\rho \frac{\partial \vec{v}}{\partial t} + \nabla \cdot \left(\rho \vec{v} \vec{v}\right) = -\nabla p + \left(\mu + \mu_t\right) \nabla^2 \vec{v} \tag{4}$$

To achieve the closure of the conservation equations, the standard k-ω mode has been used by defining the turbulent viscosity $\mu_t = \rho k/\omega$. By solving Eqs. (5) and (6), the turbulent kinetic energy k and specific dissipation rate ω can be obtained:

$$\rho \frac{\partial k}{\partial t} + \nabla \cdot \left(\rho k \vec{v}\right) = \nabla \cdot \left(\left(\mu + \frac{\mu_t}{\sigma_k}\right) \nabla k\right) + \mu_t S^2 - \rho \beta^* \omega k \tag{5}$$

$$\rho \frac{\partial \omega}{\partial t} + \nabla \cdot \left(\rho \omega \vec{v}\right) = \nabla \cdot \left(\left(\mu + \frac{\mu_t}{\sigma_\omega}\right) \nabla \omega\right) + \varpi \mu_t \frac{\omega}{k} S^2 - \rho \beta \omega^2 \tag{6}$$

S is modulus of the mean rate-of-strain tensor, $\sigma_k = \sigma_\omega = 2$, $\omega = 0.556$, $\beta = 0.075$, $\beta^* = 0.09$ [41].

The Reynolds number in the porous membrane zone is much less than 1, causing a creeping flow in the membrane. Modification has been made to the NS equations for porous membrane zone due to the additional hydraulic resistance caused by the membrane and the accumulated cake. Here, we obtain:

$$\nabla \cdot \vec{v} = 0 \tag{7}$$

$$\rho \frac{\partial \vec{v}}{\partial t} + \nabla \cdot \left(\rho \vec{v} \vec{v}\right) = -\nabla p + \mu \nabla^2 \vec{v} - \frac{\lambda \mu}{K(t)} \vec{v} \tag{8}$$

λ and $K(t)$ are the porosity and transient Darcy permeability of the porous zone, respectively. The porous zone presented in Fig. 4 is developed with a special treatment imposed on the computational domain, which has the function of modifying the Darcy permeability as the response to the filtration flux:

The porous zone is a combination of the membrane and accumulated cake in the basis of resistance-in-series law.

As only large-sized particles are assumed to be included in the feed, the reverse convective flow from membrane surface to the shell side due to the concentration polarization can be ignored, as well as the driving force loss due to osmotic pressure.

Applying the resistance-in-series law [7,42] gives:

$$J = \frac{\Delta p}{\mu \left(R_m + R_f\right)} \tag{9}$$

J, Δp, R_m and R_f are the local flux, local TMP, membrane and cake resistances, respectively.

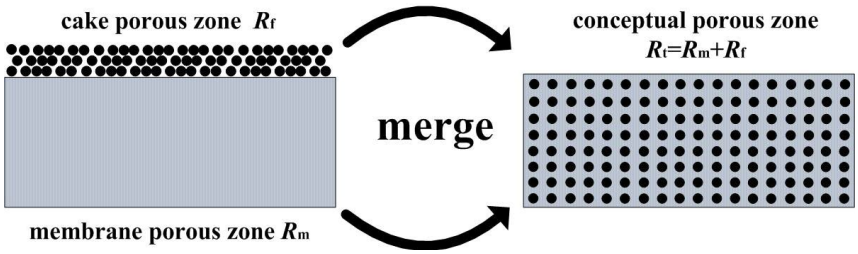

Fig. 4. Porous zone (adapted from literature [33]).

The feed is bentonite suspension, assumed to contain uniform and large sized particles. R_f has the following form [43]:

$$R_f = m\alpha \tag{10}$$

m and α are the mass of deposits per unit area and specific resistance of the cake, respectively. The equation below presents the accumulation rate of particles:

$$\frac{\partial m}{\partial t} = c_s J \frac{\phi_f - \phi_s}{\phi_f} \approx c_s J \tag{11}$$

c_s, ϕ_s and ϕ_f are the mass concentration, volume fraction of particles in the cake and feed suspension, respectively. The mass concentration was assumed to be constant in the bulk flow of shell side, independent of time. The far right-hand side of Eq. (11) is valid as dead-end filtration is often applied to dilute feed suspensions. Eq. (11) has its difference form, instituted with Eq. (10) will give:

$$\Delta R_f = \alpha c_s J \Delta t \tag{12}$$

Therefore, the expression of cake resistance is:

$$R_f(t) = \alpha c_s \left(\sum_{i=0}^{t/\Delta t-1} J(i\Delta t)\Delta t \right) \qquad \Delta t \to 0 \qquad t \geq \Delta t \tag{13}$$

$$R_f(0) = 0 \tag{14}$$

The local flux in any position of the HFMM can be expressed by combining Eqs. (9), (13) and (14):

$$J(t) = \frac{\Delta p}{\mu R_m + \mu\alpha c_s \left(\sum_{i=0}^{t/\Delta t-1} J(i\Delta t)\Delta t \right)} \qquad \Delta t \to 0 \qquad t \geq \Delta t \tag{15}$$

$$J(0) = \frac{\Delta p}{\mu R_m} \tag{16}$$

As shown in Eqs. (15) and (16), the $K(t)$ in Eq. (8) can be expressed as:

$$K(t) = \frac{\delta}{R_m + \alpha c_s \left(\sum_{i=0}^{t/\Delta t-1} J(i\Delta t)\Delta t \right)} \qquad \Delta t \to 0 \qquad t \geq \Delta t \tag{17}$$

$$K(0) = \frac{\delta}{R_m} \tag{18}$$

δ is the thickness of membrane porous zone.

The model development in the form of Eqs. (1)–(18) has been described in details in our previous study [33], which was focused on the fluid distribution and fouling process in an industrial HFMM with uniform fiber size and packing. Here again the model equations are listed as above because the fluid flows and fouling behaviors within the four HFMMs are based on the same model equations, that is, Eqs. (1)–(18), in spite of the difference in module structure among them. The rationality of Eqs. (9)–(18) is in the basis of these assumptions: the axial velocity along the hollow fiber membrane is low due to the dead-end mode, and the effect of fluid shear on the foulants transport in the axial direction is neglected; foulants follow the streamlines till they make contact with the membrane or the cake, and the molecular interaction forces allow foulants to adhere as soon as they make contact; the effect of cake layer on the width of shell channel is neglected due to the low feed concentration and short filtration cycle.

2.3. Implementation of simulations

The parameters used in the simulations are listed in Table 1. The boundary conditions presented in Fig. 3 have their form of mathematical equations [33]. The following introduction regarding the implement of simulation can also be seen from our previous study. It was presented here again for the convenience of the readers.

The simulations were conducted with the commercially available finite-volume based code Fluent 6.3.26. A coupled solver with the SIMPLE scheme was used to determine the pressure and velocity fields. The spatial discretization scheme of the pressure was second-order implicit. The spatial discretization scheme of the momentum, turbulent kinetic energy and specific dissipation rate were all second-order upwind. During each time step, the residual of the continuity fell below 1×10^{-4} and the residuals of velocity, turbulent kinetic energy and specific dissipation rate fell below 1×10^{-5}. The volumetric flow rate of permeate was monitored in real time mode. The coupling between viscous resistance of conceptual porous zone and fluid flow in the module was realized through user-defined functions. Each simulation was implemented with two Intel Xenon CPUs and 64GB of DDR4 RAM and lasted for about 6–7 weeks.

The time step size in the simulation was determined by time step size independence check. 1×10^{-3}, 5×10^{-3} and

Table 1
Parameters used in the simulations

Parameters	Symbol	Value
Darcy permeability of membrane zone, m^2	$K(0)$	4.9×10^{-16}
Porosity of membrane zone	λ	0.7
Operating temperature, °C	T	25
Shell inlet pressure, Pa	p_0'	1×10^5
Lumen outlet pressure, Pa	p_l''	0
Feed concentration, g L^{-1}	c_s	0.2
Specific resistance of the cake, m kg^{-1}	α	3×10^{14}
Time step size, s	Δt	0.01
Duration of filtration, s	t_{tot}	1,500
Residuals (continuity, velocities, turbulent kinetic energy, specific dissipation rate)	1×10^{-4}, 1×10^{-5}, 1×10^{-5}, 1×10^{-5}	
Under-relaxation factors (pressure, momentum, turbulent kinetic energy, specific dissipation rate)	0.3, 0.7, 0.8, 0.8	

1×10^{-2} s were chosen as the time steps of three separate cases. The cases were based on the same computational domain in our previous study [44]. The flux distribution at $t = 100$ s and module volumetric flow rate against time were chosen as the indexes of check. The maximum relative deviations of fluxes between neighbor time step sizes are below 0.5% and all the relative deviations of volumetric flow rates at any time are below 0.3%. It indicates that the time step size of 1×10^{-2} s is precise enough to describe the transient filtration process. Attempt has been made to increase the time step size to above 1×10^{-2} s. However, the residuals showed poor convergence of the conservation equations. Hence, the time step size of 1×10^{-2} s was finally chosen for the simulation.

2.4. Validation of CFD models

CFD simulation is based on a wide range of sub-models which are, respectively, used to describe the momentum, mass, and heat transfers and other specific processes. These models are coupled through certain numerical algorithm. It means that errors during simulation may occur due to poor choice of discretization method or drawbacks of the sub-models. Hence, validation of CFD models is a must before they are adopted to output numerical predictions regarding different cases.

In the present study, the validation has been conducted step by step. Pure water filtration experiments both within single fiber [6] and entire HFMM [34] have been performed to test the capability of present CFD models in fiber and module scales. In the single-fiber experiments, fibers with lengths of 0.095, 0.195, 0.295, 0.395 and 1 m were used for parallel tests. The volumetric flow rate obtained from CFD simulation and experiments was compared and good agreement between them was achieved. In the entire module experiment, the industrial scale HFMM containing approximately 10,000 1.92 m-active length hollow fibers was used. The CFD simulations based on the real structure of HFMM have been performed. Laminar and turbulence viscous models have been separately adopted to give different simulation results. Comparisons of volumetric flow rate/pressure drop relationship between experiment and simulations showed that the CFD model with the turbulence model agreed better with the experiment and the maximum deviation was below 5%.

In addition to consideration of the scale effect from fiber to module, the coupled process of fluid flow and fouling behavior is also a significant concern. Therefore, numerical results from the work of Serra et al. [43] which describes the increase of TMP with time during bentonite suspension filtration within a semi-scale HFMM, has been adopted to validate the CFD models. Their numerical model based on finite difference method has been validated with experiments. To validate the simulated fouling behavior, we have built dedicated semi-scale HFMM CFD model with identical geometrical and process parameters to the one adopted by Serra et al. [43]. Comparisons between the present CFD simulation results and their numerical results have been made and satisfying agreement between them has been obtained with a maximum deviation of 7%. For the conciseness of the paper, the readers are welcomed to refer to our previous works [6,33,34] for more details of the validation.

3. Results and discussion

3.1. Transient pressure and velocity contours

Pressure and velocity distributions are vital to the performance of HFMMs [45,46] as they determine the flux magnitude/distribution and fouling condition inside the HFMMs. The routine methodology of investigating the flow field within the HFMMs is treating the entire module as a porous media with certain porosity/friction distribution or representing the whole module with single element by assuming that all the fibers have identical properties. However, the treatments above may fail in capturing the realistic details of fluid distribution and fouling process, which are essential to further optimization of the HFMM structure and intensification of membrane process. In this regard, part of the simulation results is presented in Figs. 5–7 to show the flow field inside HFMMs with various fiber arrangements.

Figs. 5a–c present the transient velocity and pressure contours in three cross sections ($z = 0.1$, 0.3, 0.49 m, $z = 0$ m corresponds the axial location of inlet) at four moments

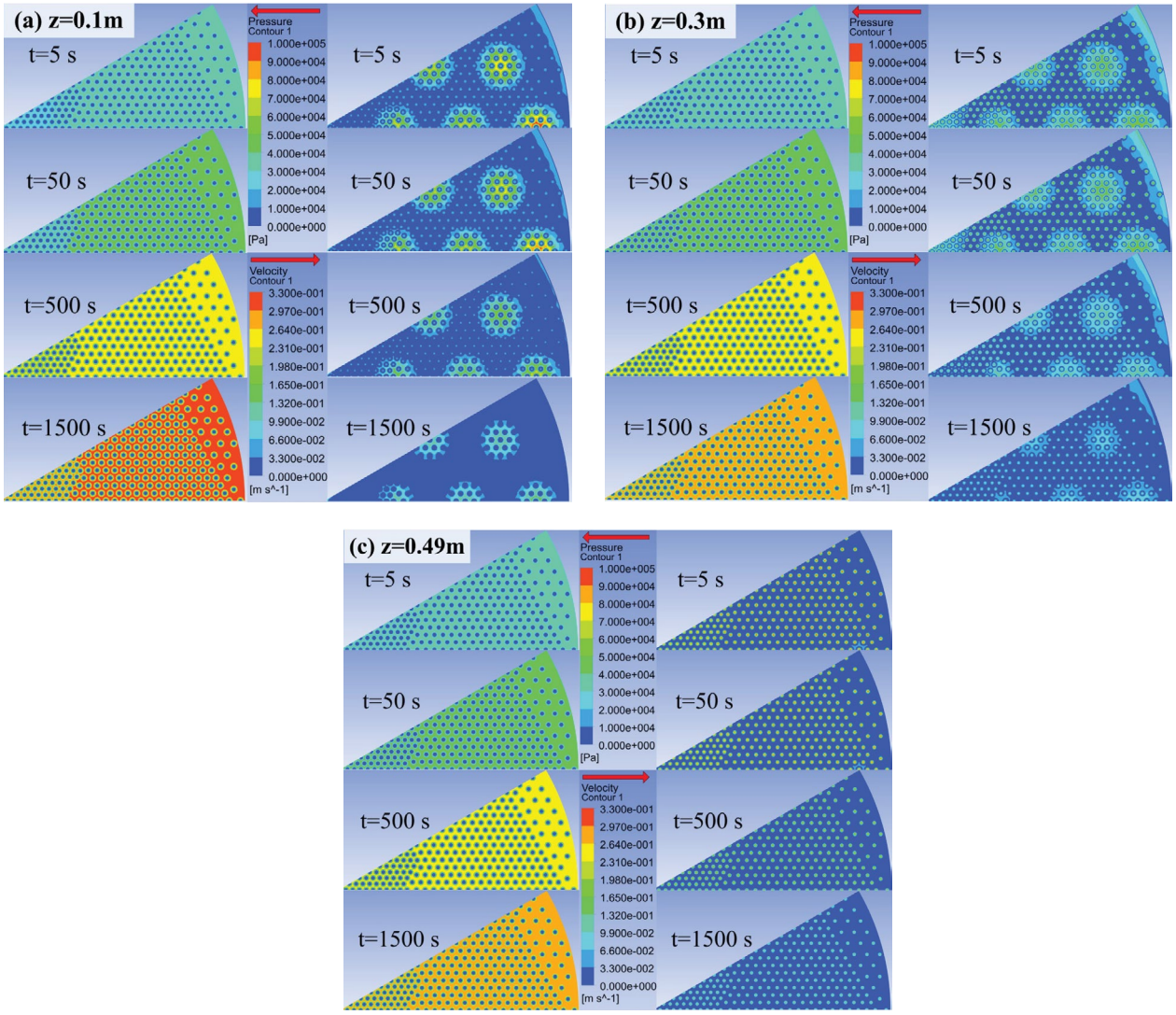

Fig. 5. Transient pressure and velocity contours of the HFMM with fiber arrangement dense to sparse radially: (a) z = 0.1 m, (b) z = 0.3 m, and (c) z = 0.49 m.

(t = 5; 50; 500; 1,500 s) in the HFMM with fiber arrangement dense to sparse radially. It is the same to Figs. 6 and 7, except for the fiber arrangement. The contours in the HFMM with uniform fiber arrangement can be seen in our previous paper [45,46]. As shown in Figs. 5–7, the pressure increases with time and this is applicable to the three cross section in any HFMM in the present study. This unexpected phenomenon has been explained in our previous study [33] that it results from dynamic evolution of energy consumption distribution between the inlet tubesheet and fiber bundle. In Fig. 5a, lower pressure exists in the region with denser fiber packing. It indicates that the region with high packing density is more likely to be the "dead-zone" and less fluid will flow through that region. In Fig. 6, similar "dead-zone" exists but is less visible than the one in Fig. 5. This is probably due to the inverse effect of wall-flow in the periphery of fiber bundle where packing density is low. In Fig. 7, the non-uniformity of pressure distribution is almost invisible. The velocity contours presented in Figs. 6 and 7 are similar in their dependence on location and time. The average velocity in the shell side decreases with time while the lumen average velocity increases because of the mass transfer between the two sides in the dead-end outside-in mode. Regions with local high velocity can be seen near the periphery of fiber bundle and axial projections of inlet openings. The former kind of local high velocity results from the low hydraulic resistance in the region with low shell void fraction. The latter one results from the axial evolution of high inlet velocity of fluid passing the tubesheet. Difference in velocity distribution among the HFMMs with various fiber arrangements can hardly be identified. Therefore, to obtain more details of the flow field, methods with higher resolution are required.

3.2. Dynamic evolution of energy consumption distribution

The inlet manifold of an HFMM can improve the initial uniformity of feed flow and divide the entire module into shell and lumen sides. However, it can also cause

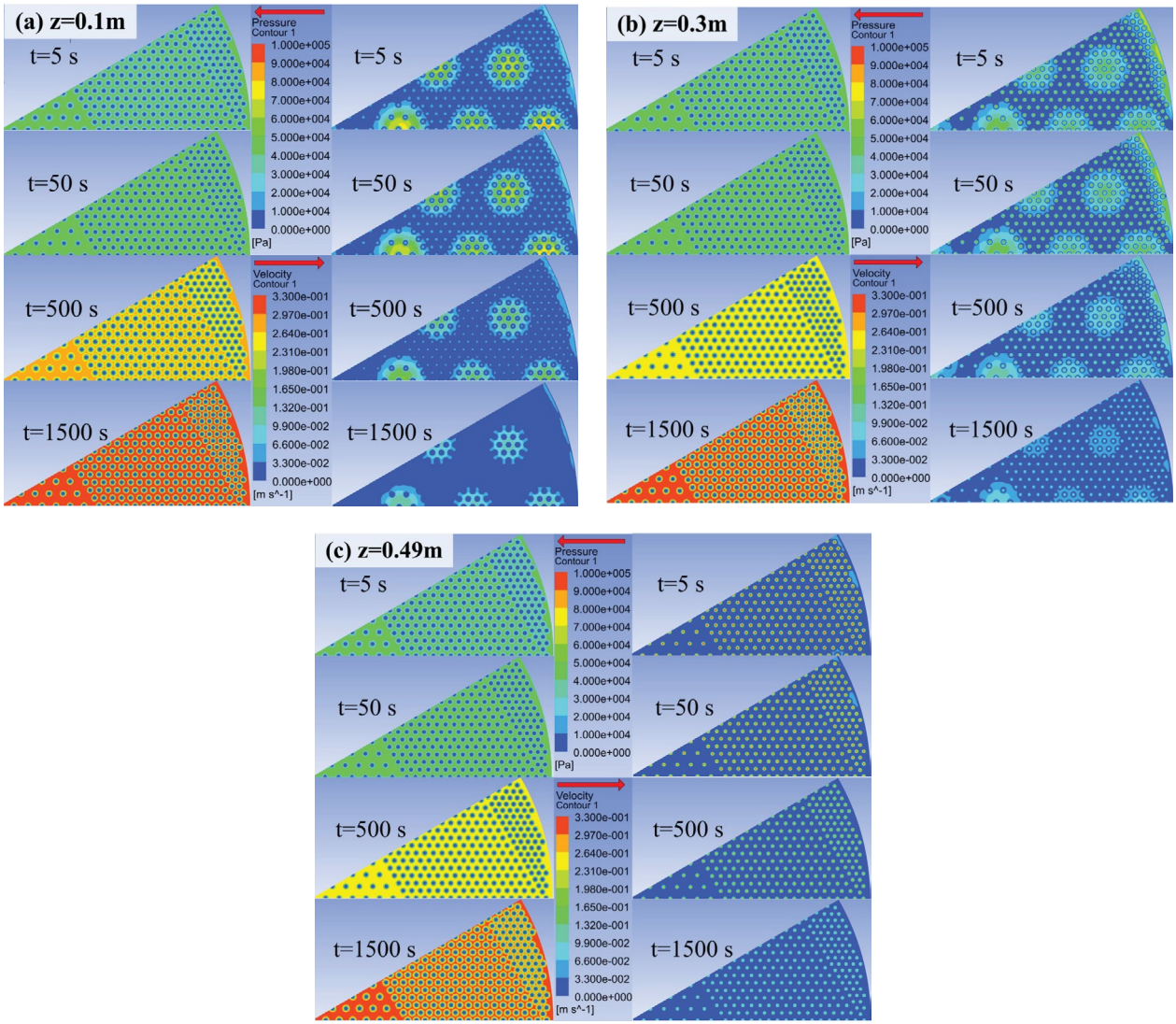

Fig. 6. Transient pressure and velocity contours of the HFMM with fiber arrangement sparse to dense radially: (a) z = 0.1 m, (b) z = 0.3 m, and (c) z = 0.49 m.

considerable energy consumption with improper structure design. For membrane engineers, it is crucial to know the individual percentage of energy consumed by each part of the HFMMs so as to assess the performance of the HFMMs in a comprehensive way. In addition, the issue of energy consumption is time dependent as the fouling process, especially in dead-end mode, evolves with time. Here we present the proportion of energy consumption for the inlet manifold and fiber bundle against time for the HFMMs with different fiber arrangement in Fig. 8. n is the number of fibers inside a certain HFMM.

The overall pressure drop of the HFMM is set to 1×10^5 Pa. Part of energy is stored or transformed as fluid flows along the module length overcoming the gravity, which is reversible. Hence, the irreversible part of energy consumed, that is, overall energy consumption, is 9.5104×10^4. As shown in Fig. 8, regardless of the fiber arrangement, the part of energy consumed by the inlet manifold decreases while the one by the fiber bundle increases. As described in our previous study [33], the time dependence of the energy consumption distribution results from two factors. The energy consumed by inlet manifold is mainly due to inertial resistance which is proportional to the square of volumetric flow rate, while the fiber bundle causes mainly the viscous resistance which is proportional to the first power of volumetric flow rate. Therefore, as the flow rate of module decreases, the energy consumption of inlet manifold decreases faster than the one of fiber bundle. The flow rate of four HFMMs with time can be seen in Fig. 9. The other factor is the fouling caused increase in the resistance coefficient for the fiber bundle. As for the inlet manifold, the resistance coefficient is nearly constant within certain range of Reynolds number.

It is noticeable that the fiber arrangement has an impact on the energy consumption distribution between the inlet manifold and fiber bundle. To be precise, higher proportion of energy will be consumed by the fiber bundle in the HFMM with fiber arrangement sparse to dense radially than the other HFMMs, especially the HFMM with reverse fiber

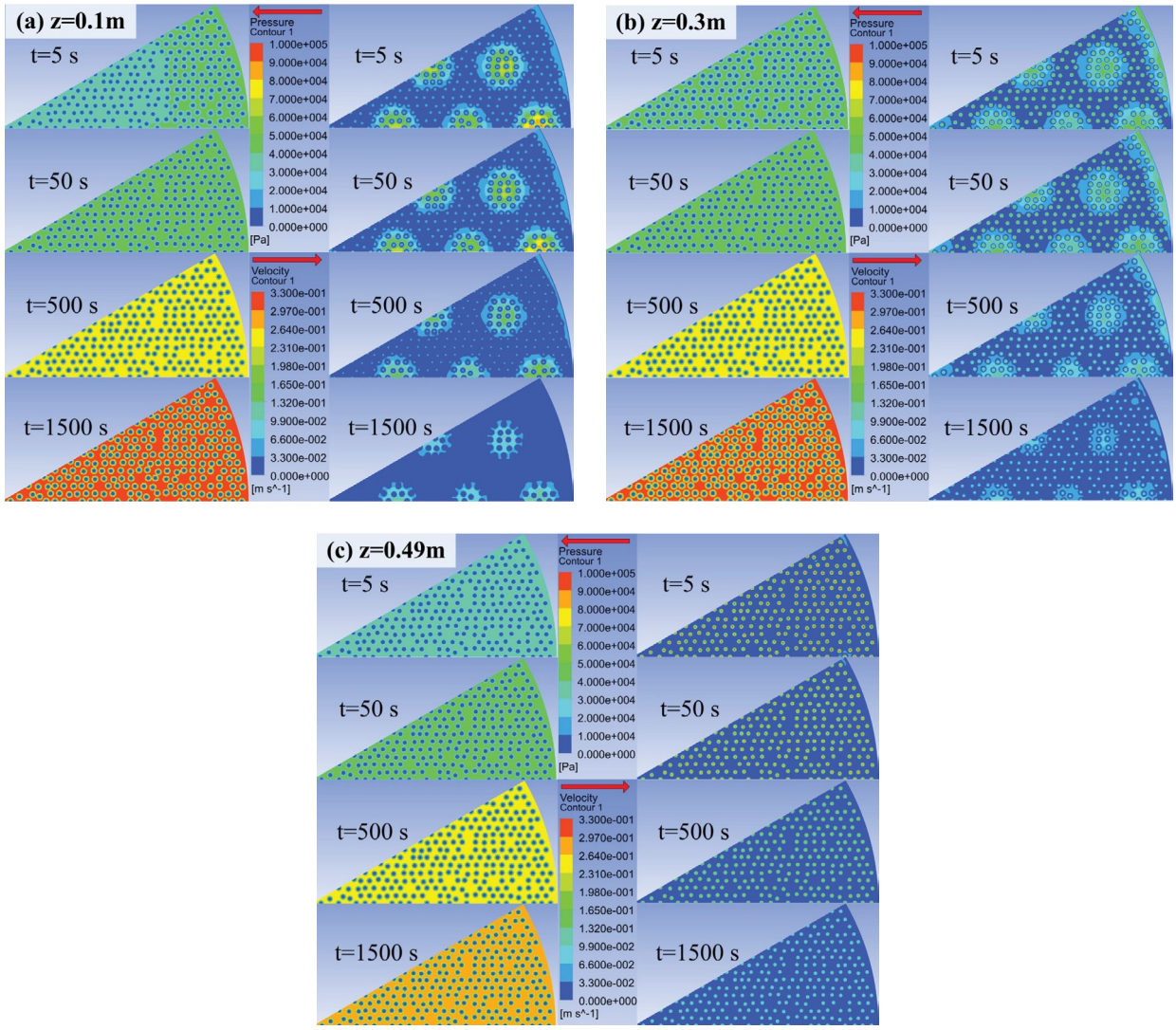

Fig. 7. Transient pressure and velocity contours of the HFMM with random fiber packing: (a) $z = 0.1$ m, (b) $z = 0.3$ m, and (c) $z = 0.49$ m.

arrangement, that is, dense to sparse radially. The result of this impact causes diversity of volumetric flow rate among the four HFMMs, as shown in Fig. 9. By comparing Figs. 9 with 8, it can be seen that the HFMM with higher proportion of energy consumption by fiber bundle will have a higher volumetric flow rate, corresponding to higher energy efficiency.

It indicates that the HFMM with non-ideal structure (non-uniform fiber arrangement), which a lot of membrane engineers has studied for various application [18,24,30,47], does not definitely present low performance, at least it is not the case in the present study. It can be inferred that the fiber arrangement sparse to dense radially has offset the impact of wall flow near the periphery of fiber bundle with relatively lower packing density while the fiber arrangement dense to sparse radially has strengthened the impact of wall flow. Therefore, the fiber arrangement sparse to dense radially has an advantage over the ideal or random fiber arrangement in terms of increasing the energy efficiency.

To further analyze the cause of diversity in energy efficiency for HFMMs with different fiber arrangement, as well as to present more information of the flow field, the shell and lumen pressure distributions inside the HFMMs have been plotted against time, as shown in Fig. 10. For each HFMM, three typical shell regions have been selected. In the lumen side, as indicated in Fig. 10d, the axial distributions of lumen pressure of all the fibers at certain time nearly follow the same profile. It means the axial distribution of lumen pressure of certain HFMM can be represented with the one of arbitrary singular fiber thereof, as has been done for Figs. 10a–c. As shown in Fig. 10, the shell and lumen pressures both decrease in the axial direction, forming the driving force of fluid flow in each region. However, as time passes, the shell pressure increases whereas the lumen pressure decreases. This difference results from the mechanism behind the pressure dynamic evolution in the two regions. The increase in shell pressure is due to the resistance redistribution between fiber bundle and inlet manifold whereas the decrease in lumen pressure is due to the decline in volumetric flow rate. It means that every local TMP (Δp) keeps increasing with time. However, it appears that the filtration

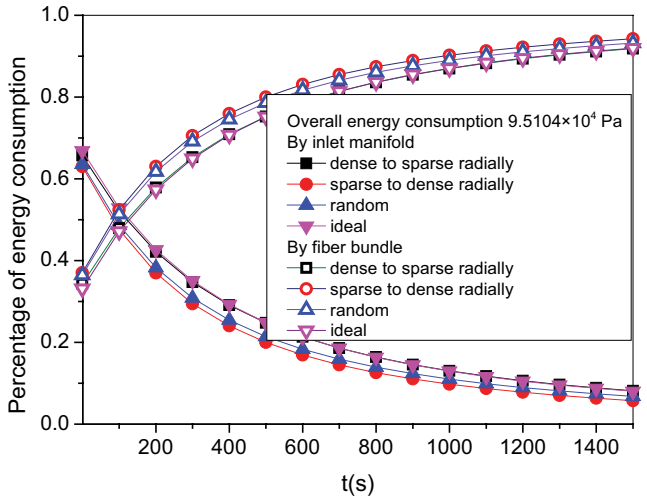

Fig. 8. Energy consumption distribution against time within different HFMMs.

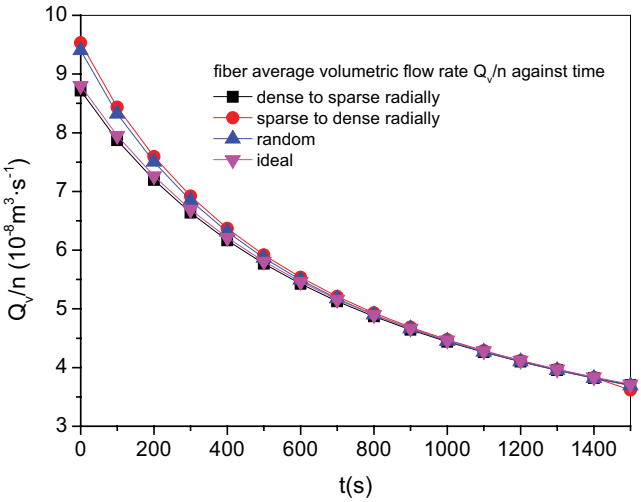

Fig. 9. Fiber average volumetric flow rate of different HFMMs against time.

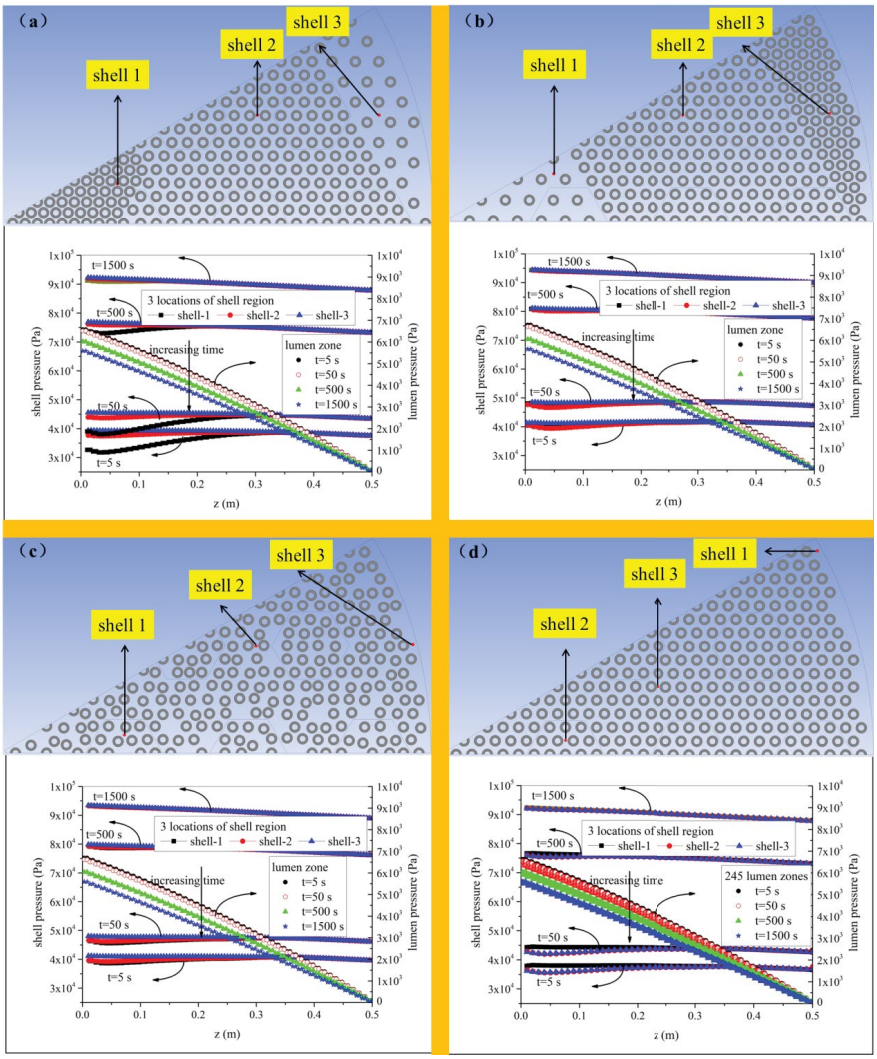

Fig. 10. Spatial variation of the pressure at any location inside the lumen and in the shell side for different fiber arrangement at different time. (a) dense to sparse radially, (b) sparse to dense radially, (c) random, and (d) ideal (adapted from literature [33]).

resistance increases faster than the filtration driving force, as indicated by the continuous decline in volumetric flow rate.

Differences in pressure profiles can be seen in Fig. 10 that the pressure distribution in HFMM with fiber arrangement sparse to dense radially is much more uniform than the HFMM with fiber arrangement dense to sparse radially. In addition, the average pressure of the former HFMM is higher than the latter one. The differences can serve as the proof of the aforementioned inference, that is, the impact of wall flow near the periphery of HFMM has been offset with densely packed fiber bundle. The energy efficiency of HFMMs will be improved with more uniform pressure distribution.

3.3. Dynamic evolution of flux and cake distributions

The dynamic evolution of flux/cake mass and their distributions is inevitable during the filtration as the foulants accumulation on the membrane surface makes the process time dependent. Such phenomena have been reported widely in literature [7,48,49]. As has been mentioned in our previous study [33], most of the related studies are focused on single-fiber system [7,48] with axial flux/cake distribution along the fiber length. However, flux/cake distribution in a HFMM has three-dimensional non-uniformity, which is also affected by the fiber arrangement. Here we present the fiber average flux/cake mass of all the fibers in HFMMs with different fiber arrangement (excluding the HFMM with uniform fiber arrangement). By exporting and postprocessing simulation data, the fiber or length average flux/cake mass at different moments (t = 0 or 5; 500; 1,500 s) can be obtained, based on which the top 50 (highest flux/cake mass) and bottom 50 (lowest flux/cake mass) fibers have been labeled with red or yellow triangles, respectively, as shown in Figs. 11–13.

In Fig. 11, the top-50-flux fibers are located at the periphery of fiber bundle at t = 0 s. In that region, the shell void fraction is higher than the one inside the fiber bundle. Hence, higher shell flow rate exists near the housing wall, forming the wall flow, and the fiber arrangement dense to sparse radially has made the wall flow more serious. This wall flow can be found in Figs. 5–7. High fluid velocity causes high shell pressure due to the conversion from dynamic pressure to static pressure; thus increasing the local flux of fibers located at that region. In contrast, the region near the center of module, where fibers are densely packed and no wall flow exists, contains the bottom 50 fibers with the lowest flux. At t = 5 s, the cake distribution, especially in terms of the top/bottom 50 fibers with extreme cake mass, is nearly the same to the flux distribution at t = 0 s. This is because the high/low local flux results in high/low foulants accumulation rate and more/less cake mass with certain duration. As time passes, the top 50 fibers tend to migrate to the center of fiber bundle while the bottom 50 fibers tend to migrate in opposite direction. However, the cake distribution appears to be almost unchanged. At t = 1,500 s, the end of the filtration, the fibers with extreme flux have finished their migration while the cake distribution is still with little change. The two different dynamic evolutions reveal the interaction between the flux and cake distributions. High flux will cause high cake mass while high cake mass will cause low flux. At initial state of the filtration, the flux of each fiber

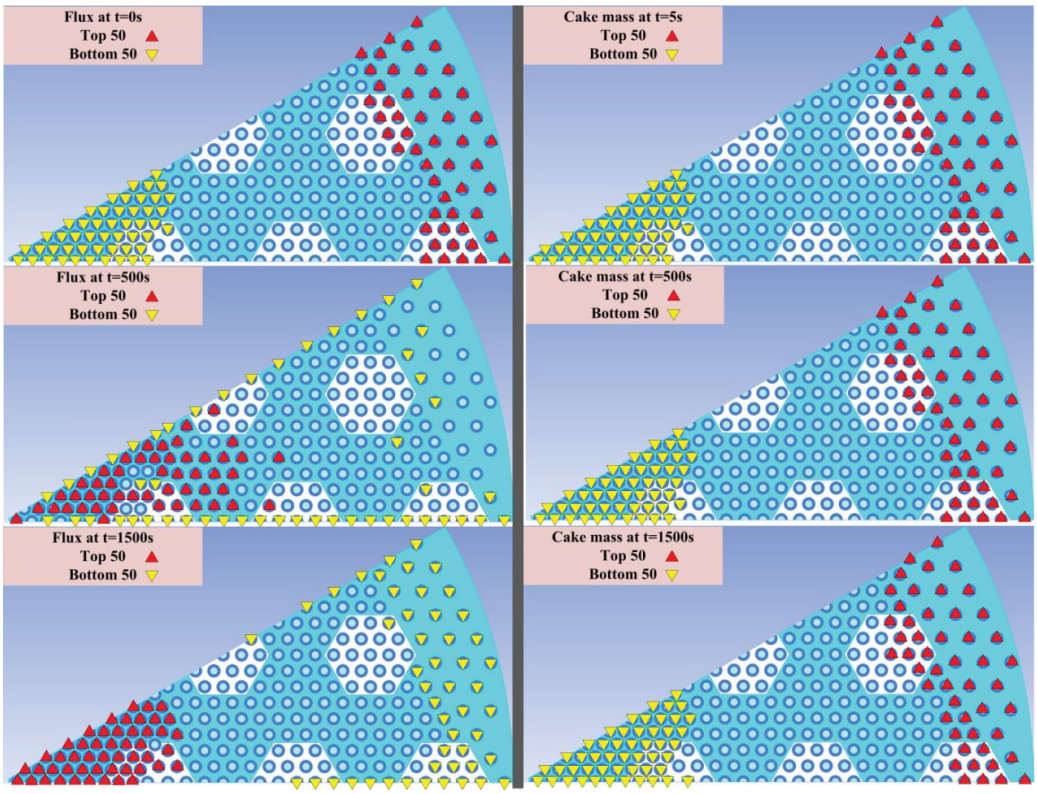

Fig. 11. Flux and cake distributions against time in the HFMM with fiber arrangement dense to sparse radially.

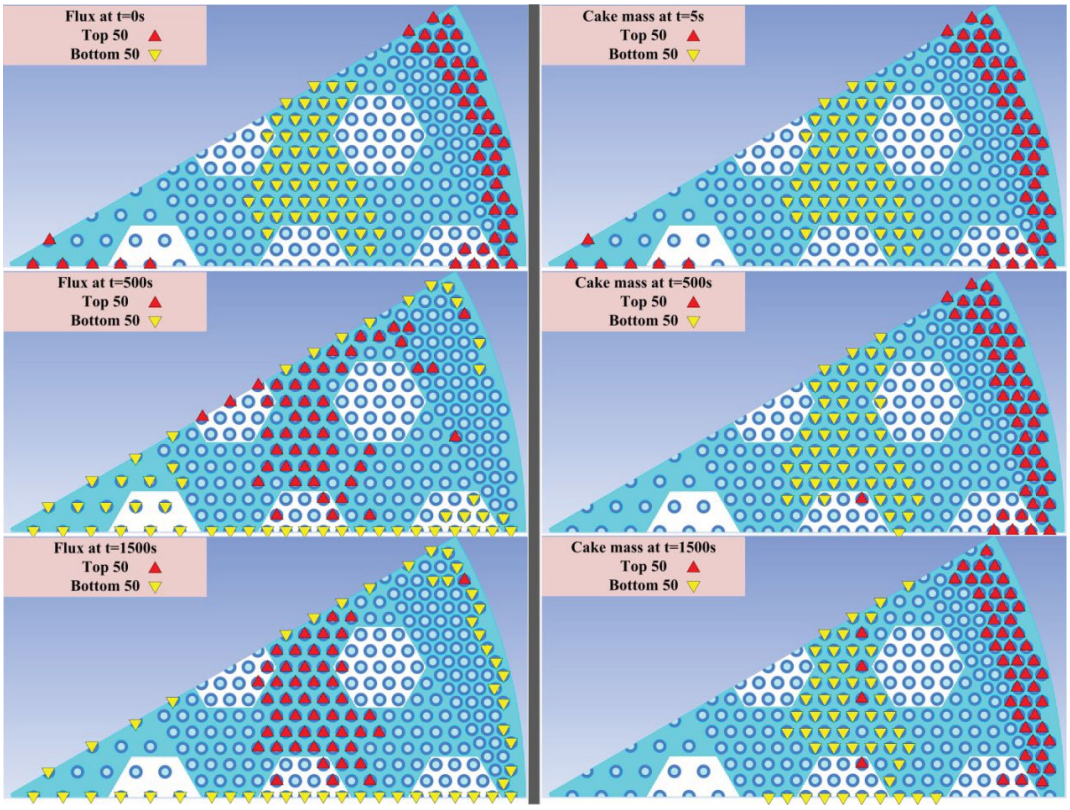

Fig. 12. Flux and cake distributions against time in the HFMM with fiber arrangement sparse to dense radially.

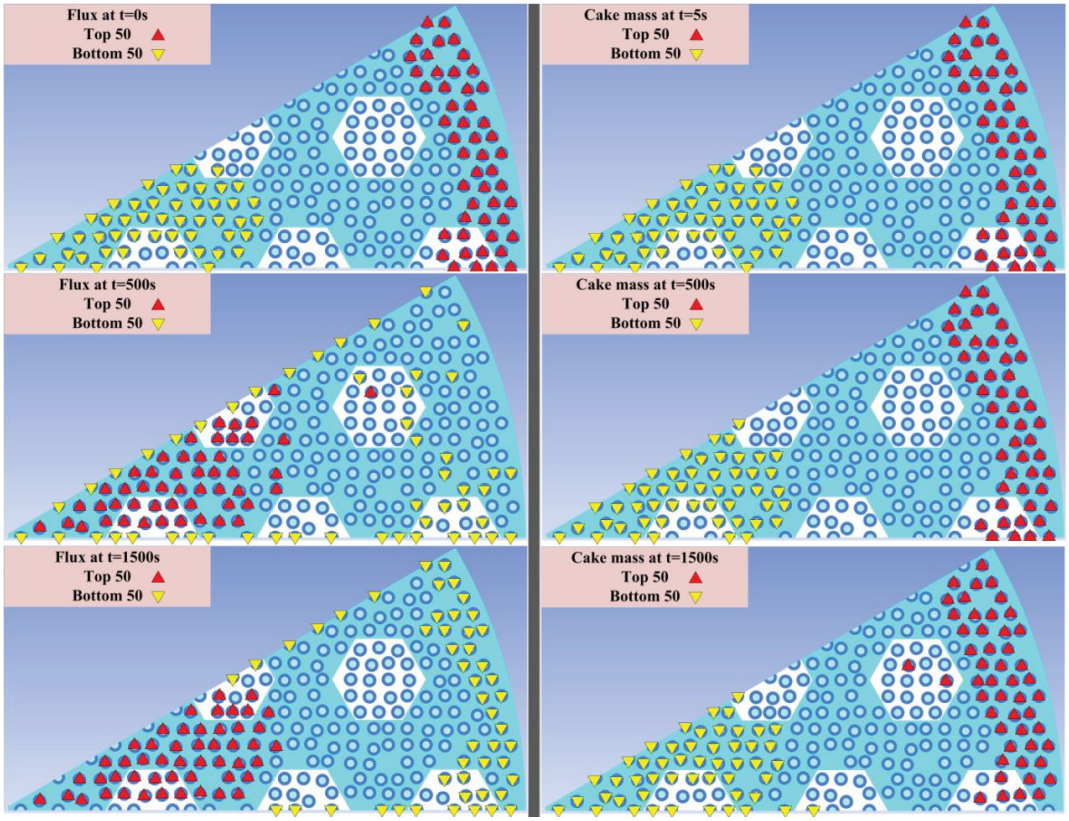

Fig. 13. Flux and cake distributions against time in the HFMM with random fiber packing.

is high as no foulants have accumulated on the membrane surface. The initial flux distribution has determined the initial cake distribution and any subsequent modification of the cake distribution due to foulants accumulation is almost ignorable as the flux keeps declining. Finally, the fixed cake distribution causes remarkable change to the flux distribution through manipulating the filtration resistance distribution, as shown in Fig. 11.

By referring to Figs. 11–13, except for the difference in initial flux and cake distribution due to the diversity of fiber arrangement, the dynamic evolution modes of flux and cake distributions among the three HFMMs are similar to each other, which means the description above and the mechanism behind it has wide application potential, regardless of the fiber arrangement. In other words, for any type of hollow fiber ultrafiltration/microfiltration module, the final distribution of foulants inside the module will be similar to the initial flux distribution. As the initial flux distribution is purely a function of geometrical parameters, one of the applications is to help membrane researchers to establish the relationship between module structure and fouling behavior. It can also contribute to improving understanding of membrane fouling behavior from a scientific point. In industrial application, it will be beneficial to the design of washing strategy to different type of HFMMs since the foulants distribution is predicable.

3.4. Water productivity of the HFMMs with different fiber arrangement

In Fig. 14, the reciprocal of fiber average volumetric flow rate has been plotted against fiber average water production for the four HFMMs with different fiber arrangement. The deviations of results between CFD simulation and model prediction have been presented in Fig. 14. The 15 points along each line correspond 15 moments during the filtration: 100 s to 1,500 s with the interval of 100 s. As shown in Fig. 14, the four lines are nearly linear which means the relationship between the two said parameters can be expressed with a linear equation. This equation has been developed in our previous study [33], which is applicable to the HFMM with ideal structure. The mathematical expression can be seen in Eq. (19).

$$\frac{ndt}{dV}=\frac{0.6\mu c_s\alpha}{(\mathrm{TMP})_t\left[\left(A_i+A_e\right)/2\right]^2 d_i/d_e}\frac{V}{n}+\frac{1.26\left\{\left(\sigma^2+\chi^2\right)\cosh\left(\theta L\right)+\sigma\chi\left[2+\theta L\sinh\left(\theta L\right)\right]\right\}}{(\mathrm{TMP})_t\left[\theta\left(\sigma+\chi\right)\sinh\left(\theta L\right)\right]} \tag{19}$$

In Eq. (19), $\theta=\sqrt{\gamma(\sigma+\chi)}$, $\gamma=\frac{\pi d_e}{\mu R_m}$, $\sigma=\frac{8\mu g(\varepsilon)(1-\varepsilon)^2}{\pi\varepsilon^2 d_e^4}$, $\chi=\frac{128\mu}{\pi d_i^4}$, $g(\varepsilon)=\frac{8\varepsilon^2}{2(1-\varepsilon)-\ln(1-\varepsilon)-(1-\varepsilon)^2/2-1.5}$. ε, A_i, A_e, d_i, d_e, L are the average shell void fraction, internal and external surface areas of fiber, internal and external diameters of fiber, fiber length, respectively. The most attractive parameter in Eq. (19) is $(\mathrm{TMP})_t$, which makes Eq. (19) special from common equations. First, TMP represents the part of energy consumed by fiber bundle. Second, the subscript t means that TMP is a time-dependent parameter as dt/dV and V. For instance, in the HFMM with random fiber arrangement, $(\mathrm{TMP})_t$ is 48,860 Pa at t = 100 s and 84,645 Pa at t = 1,000 s.

To test if Eq. (19) is applicable to the other three HFMMs, data analysis has been performed by substituting the time-dependent parameters $(\mathrm{TMP})_t$ and V/n into Eq. (19) for each HFMM and making comparison of ndt/dV between CFD

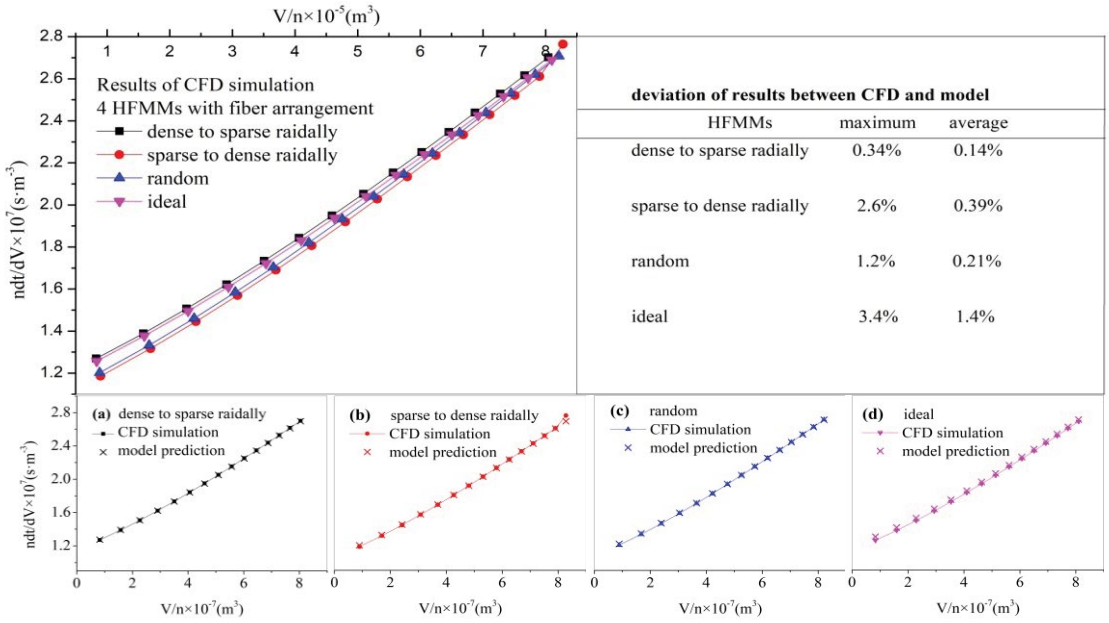

Fig. 14. Relation between reciprocal of the fiber average volumetric flow rate and fiber average water production obtained through simulation and model (Eq. (19)).

and model (Eq. (19)). As shown in Fig. 14, the maximum and average deviations between the two results for each HFMM have been listed in the right part of Fig. 14. It is noticeable that the deviations are very low, proving that Eq. (19) can smoothly describe the water productivity of HFMMs with different fiber arrangement.

Eq. (19) can be used to assess whether a HFMM is well designed or not. Any HFMM with the similar structure as the ones in the present study can be analyzed in dead-end outside-in filtration. During the experiment, by measuring the time-dependent parameters dt/dV and V of a HFMM and substituting them together with other geometrical parameters of the HFMM into Eq. (19), the energy consumption of fiber bundle at any time can be obtained. With the above information, the energy consumed by inlet manifold is obtainable and whether the HFMM is energy-efficient can be judged. The present study on the performance of HFMMs with different fiber arrangement, especially Fig. 14, has demonstrated the application potential of Eq. (19) for HFMMs with non-ideal fiber arrangement.

4. Conclusion

The novelty of present work lies in the investigation of how fiber arrangement affects the performance of industrial-scale HFMMs. Different from most of the previous work focused on HFMMs with various random fiber packing [16,18–20,24,29,30,32], the present work has attempted to investigate the optimized pattern of the fiber arrangement in terms of improving the performance of HFMMs through three-dimensional transient simulation. The HFMM with fiber arrangement sparse to dense radially has higher energy efficiency than the other three HFMMs since the densely packed fibers near the housing wall weaken the effect of wall flow. However, the flux/cake distributions inside the four HFMMs have shown similarity in their modes of dynamic evolution, despite the difference in fiber arrangement among them. The model used to describe the water productivity of HFMMs has been demonstrated to have wide application potential for HFMMs with different fiber arrangement.

Acknowledgments

The authors are thankful for the financial support from the National Natural Science Foundation of China (21706066). The authors also gratefully acknowledge financial support from China Scholarship Council (201906745003).

Symbols

A_e — Membrane external surface area, m^2
A_i — Membrane internal surface area, m^2
c_s — Mass of solid per unit volume of the feed suspension, g L^{-1}
d_e — External diameter of hollow fiber membrane, mm
d_i — Internal diameter of hollow fiber membrane, mm
J — Local flux, $m^3\ m^{-2}\ s^{-1}$
$K(t)$ — Time-dependent Darcy permeability of porous zone, m^2
K_m — Permeability of membrane, m^2
L — Length of hollow fiber membrane, m
m — Mass of deposits per unit area, kg m^{-2}
Δp — Local trans-membrane pressure, Pa
p_0' — Pressure of shell inlet, Pa
p_L'' — Pressure of lumen outlet, Pa
Q_v — Volumetric flow rate, $m^3\ s^{-1}$
R_f — Cake resistance, m^{-1}
R_m — Membrane resistance, m^{-1}
R_t — Total resistance, m^{-1}
V — Water production, m^3
α — Specific resistance of the cake, m kg^{-1}
δ — Thickness of the porous membrane, mm
ε — Shell void fraction
λ — Porosity of porous membrane
ϕ_f — Volume fraction of solid in the feed suspension
ϕ_s — Volume fraction of solid in the cake

References

[1] M.A. Monfared, N. Kasiri, T. Mohammadi, A CFD model for prediction of critical electric potential preventing membrane fouling in oily waste water treatment, J. Membr. Sci., 539 (2017) 320–328.
[2] E. Drioli, G. Di Profio, E. Curcio, Membrane-Assisted Crystallization Technology, World Scientific, Singapore, 2015.
[3] Z. Ze, J. Sx, Hollow fiber membrane contactor absorption of CO_2 from the flue gas: review and perspective, Glob. Nest J., 16 (2014) 355–374.
[4] K. He, S. Chen, C. Huang, L. Zhang, Fluid flow and mass transfer in an industrial-scale hollow fiber membrane contactor scaled up with small elements, Int. J. Heat Mass Tran., 127 (2018) 289–301.
[5] M. Wang, S. Mondal, I.M. Griffiths, The role of fouling in optimizing direct-flow filtration module design, Chem. Eng. Sci., 163 (2017) 215–222.
[6] L. Zhuang, H. Guo, P. Wang, G. Dai, Study on the flux distribution in a dead-end outside-in hollow fiber membrane module, J. Membr. Sci., 495 (2015) 372–383.
[7] J. Günther, D. Hobbs, C. Albasi, C. Lafforgue, A. Cockx, P. Schmitz, Modeling the effect of packing density on filtration performances in hollow fiber microfiltration module: a spatial study of cake growth, J. Membr. Sci., 389 (2012) 126–136.
[8] I. Noda, D.G. Brown-West, C.C. Gryte, Effect of flow maldistribution on hollow fiber dialysis — experimental studies, J. Membr. Sci., 5 (1979) 209–225.
[9] J.C. Kim, J.H. Kim, J. Sung, H. Kim, E. Kang, S.H. Lee, J.K. Kim, H.C. Kim, B.G. Min, C. Ronco, Effects of arterial port design on blood flow distribution in hemodialyzers, Blood Purif., 28 (2009) 260–267.
[10] A. Frank, G.G. Lipscomb, M. Dennis, Visualization of concentration fields in hemodialyzers by computed tomography, J. Membr. Sci., 175 (2000) 239–251.
[11] Y. Wang, F. Chen, Y. Wang, G. Luo, Y. Dai, Effect of random packing on shell-side flow and mass transfer in hollow fiber module described by normal distribution function, J. Membr. Sci., 216 (2003) 81–93.
[12] V. Chen, M. Hlavacek, Application of Voronoi tessellation for modeling randomly packed hollow-fiber bundles, AIChE J., 40 (1994) 606–612.
[13] J.D. Rogers, R.L. Long Jr., Modeling hollow fiber membrane contactors using film theory, Voronoi tessellations, and facilitation factors for systems with interface reactions, J. Membr. Sci., 134 (1997) 1–17.
[14] J. Wu, V. Chen, Shell-side mass transfer performance of randomly packed hollow fiber modules, J. Membr. Sci., 172 (2000) 59–74.
[15] L. Bao, G.G. Lipscomb, Well-developed mass transfer in axial flows through randomly packed fiber bundles with constant wall flux, Chem. Eng. Sci., 57 (2002) 125–132.

[16] L. Bao, G. Glenn Lipscomb, Mass transfer in axial flows through randomly packed fiber bundles with constant wall concentration, J. Membr. Sci., 204 (2002) 207–220.
[17] W. Ding, D. Gao, Z. Wang, L. He, Theoretical estimation of shell-side mass transfer coefficient in randomly packed hollow fiber modules with polydisperse hollow fiber outer radii, J. Membr. Sci., 284 (2006) 95–101.
[18] L. Zhang, Heat and mass transfer in a randomly packed hollow fiber membrane module: a fractal model approach, Int. J. Heat Mass Tran., 54 (2011) 2921–2931.
[19] J. Zheng, Y. Xu, Z. Xu, Flow distribution in a randomly packed hollow fiber membrane module, J. Membr. Sci., 211 (2003) 263–269.
[20] J. Zheng, Z. Xu, J. Li, S. Wang, Y. Xu, Influence of random arrangement of hollow fiber membranes on shell side mass transfer performance: a novel model prediction, J. Membr. Sci., 236 (2004) 145–151.
[21] J. Happel, Viscous flow relative to arrays of cylinders, AIChE J., 5 (1959) 174–177.
[22] M. Kostoglou, A.J. Karabelas, On the structure of the single-phase flow field in hollow fiber membrane modules during filtration, J. Membr. Sci., 322 (2008) 128–138.
[23] S. Buetehorn, D. Volmering, K. Vossenkaul, T. Wintgens, M. Wessling, T. Melin, CFD simulation of single-and multi-phase flows through submerged membrane units with irregular fiber arrangement, J. Membr. Sci., 384 (2011) 184–197.
[24] W. Li, J. Liu, L. He, J. Liu, S. Sun, Z. Huang, X. Liang, D. Gao, W. Ding, Simulation and experimental study on the effect of channeling flows on the transport of toxins in hemodialyzers, J. Membr. Sci., 501 (2016) 123–133.
[25] H. Chen, C. Cao, L. Xu, T. Xiao, G. Jiang, Experimental velocity measurements and effect of flow maldistribution on predicted permeator performances, J. Membr. Sci., 139 (1998) 259–268.
[26] J. Lemanski, G.G. Lipscomb, Effect of shell-side flows on hollow-fiber membrane device performance, AIChE J., 41 (1995) 2322–2326.
[27] L. Bao, B. Liu, G.G. Lipscomb, Entry mass transfer in axial flows through randomly packed fiber bundles, AIChE J., 45 (1999) 2346–2356.
[28] J. Lemanski, G.G. Lipscomb, Effect of shell-side flows on the performance of hollow-fiber gas separation modules, J. Membr. Sci., 195 (2002) 215–228.
[29] L. Bao, G.G. Lipscomb, Effect of random fiber packing on the performance of shell-fed hollow-fiber gas separation modules, Desalination, 146 (2002) 243–248.
[30] P. Keshavarz, S. Ayatollahi, J. Fathikalajahi, Mathematical modeling of gas–liquid membrane contactors using random distribution of fibers, J. Membr. Sci., 325 (2008) 98–108.
[31] S. Chang, A.G. Fane, T.D. Waite, A. Yeo, Unstable filtration behavior with submerged hollow fiber membranes, J. Membr. Sci., 308 (2008) 107–114.
[32] S. Huang, M. Yang, S. Chen, Effects of the random distributions on the longitudinal transport phenomena between an elliptical hollow fiber membrane bundle, J. Membr. Sci., 471 (2014) 362–371.
[33] L. Zhuang, G. Dai, Z. Xu, Three-dimensional simulation of the time-dependent fluid flow and fouling behavior in an industrial hollow fiber membrane module, AIChE J., 64 (2018) 2655–2669.
[34] L. Zhuang, H. Guo, G. Dai, Z. Xu, Effect of the inlet manifold on the performance of a hollow fiber membrane module-A CFD study, J. Membr. Sci., 526 (2017) 73–93.
[35] J. Günther, P. Schmitz, C. Albasi, C. Lafforgue, A numerical approach to study the impact of packing density on fluid flow distribution in hollow fiber module, J. Membr. Sci., 348 (2010) 277–286.
[36] X. Li, J. Li, Z. Cui, Y. Yao, Modeling of filtration characteristics during submerged hollow fiber membrane microfiltration of yeast suspension under aeration condition, J. Membr. Sci., 510 (2016) 455–465.
[37] W. Ding, L. He, G. Zhao, X. Luo, M. Zhou, D. Gao, Effect of distribution tabs on mass transfer of artificial kidney, AIChE J., 50 (2004) 786–790.
[38] H.I. Mahon, Permeability Separatory Apparatus and Process Utilizing Hollow Fibers, US Patents 3,228,877, 1966.
[39] P.J. Roache, P.M. Knupp, Completed Richardson Extrapolation, Commun. Numer. Methods Eng., 9 (1993) 365–374.
[40] K.B. Lim, P.C. Wang, H. An, S.C.M. Yu, Computational Studies for the Design Parameters of Hollow Fibre Membrane Modules, J. Membr. Sci., 529 (2017) 263–273.
[41] FLUENT User's Guide, Fluent Inc., 2006.
[42] B. Tansel, W.Y. Bao, I.N. Tansel, Characterization of fouling kinetics in ultrafiltration systems by resistances in series model, Desalination, 129 (2000) 7–14.
[43] C. Serra, M.J. Clifton, P. Moulin, J. Rouch, P. Aptel, Dead-end ultrafiltration in hollow fiber modules: module design and process simulation, J. Membr. Sci., 145 (1998) 159–172.
[44] L. Zhuang, G. Dai, Numerical simulation of dynamic process during outside-in dead-end filtration in hollow fiber membrane module, CIESC J., 67 (2016) 2841–2850.
[45] J. Wang, X. Gao, G. Ji, X. Gu, CFD simulation of hollow fiber supported NaA zeolite membrane modules, Sep. Purif. Technol., 213 (2019) 1–10.
[46] D. Kim, M. Kwak, K. Kim, Y.K. Chang, Turbulent jet-assisted microfiltration for energy efficient harvesting of microalgae, J. Membr. Sci., 575 (2019) 170–178.
[47] Z. Li, L. Zhang, Flow maldistribution and performance deteriorations in a counter flow hollow fiber membrane module for air humidification/dehumidification, Int. J. Heat Mass Tran., 74 (2014) 421–430.
[48] X. Li, J. Li, J. Wang, H. Wang, B. He, H. Zhang, W. Guo, H.H. Ngo, Experimental investigation of local flux distribution and fouling behavior in double-end and dead-end submerged hollow fiber membrane modules, J. Membr. Sci., 453 (2014) 18–26.
[49] M. Lee, J. Kim, Analysis of local fouling in a pilot-scale submerged hollow-fiber membrane system for drinking water treatment by membrane autopsy, Sep. Purif. Technol., 95 (2012) 227–234.